Ultrastrong magnon-magnon coupling in synthetic antiferromagnets induced by interlayer Dzyaloshinskii-Moriya interaction

Yuqiang Wang,[1,2,*] Jihao Xia,[1,2,*] Caihua Wan,[1,2] Xiufeng Han,[1,2,3,†] and Guoqiang Yu[1,2,3,‡]

[1]*Beijing National Laboratory for Condensed Matter Physics, Institute of Physics, Chinese Academy of Sciences, Beijing 100190, China*

[2]*Center of Materials Science and Optoelectronics Engineering, University of Chinese Academy of Sciences, Beijing 100049, China*

[3]*Songshan Lake Materials Laboratory, Dongguan, Guangdong 523808, China*

(Received 13 June 2023; revised 22 December 2023; accepted 22 December 2023; published 13 February 2024)

Recently, there has been significant interest in magnon-magnon hybrid systems in the field of spintronics due to their potential for quantum engineering. Achieving strong coupling, and even ultrastrong coupling (USC), is crucial for enhancing the efficiency of quantum information processing. While the strong coupling has been widely observed in magnon-magnon hybrid systems, the USC has been rarely reported. Therefore, the current focus of research is to explore more possible mechanisms for realizing magnon-magnon USC. Here, we highlight that the interlayer Dzyaloshinskii-Moriya interaction (DMI) can break the rotation symmetry in synthetic antiferromagnets (SAFs) when the DMI vector **D** is nonorthogonal to the external dc magnetic field. As a result, magnon-magnon coupling can be induced by the interlayer DMI, as confirmed by both macrospin model and micromagnetic simulations. We suggest that the strength of magnon-magnon coupling can be tuned to a considerable degree by properly selecting the direction of **D** and adjusting the material parameters of SAF, such as the magnetic anisotropy field, the effective interlayer DMI field, and the effective Ruderman-Kittel-Kasuya-Yosida interaction field. Surprisingly, a sudden increase of coupling strength takes place when the total magnetic anisotropy field changes the sign. We emphasize that within this region, the coupling properties exhibit high sensitivity to anisotropy, and even an extremely small interlayer DMI intensity can induce the USC. The maximum normalized coupling strength in this region can surpass 0.5, which is far in excess of the commonly used value 0.1 that is considered as a requirement for establishing USC. These results place SAFs with interlayer DMI in focus for the future study of magnon-magnon USC, which can be of considerable interest for the experimental research.

DOI: 10.1103/PhysRevB.109.054416

I. INTRODUCTION

Synthetic antiferromagnets (SAFs), which consist of two magnetic subsystems linked by the Ruderman-Kittel-Kasuya-Yosida (RKKY) interaction [1], have been extensively investigated over the past few decades [2–15]. Due to the antiferromagnetic nature of the RKKY interaction in SAFs, these systems exhibit higher resonance frequencies compared to traditional ferromagnets, making them attractive for magnetic random-access memories [16]. When the inversion symmetry is broken, a higher-order interaction, the Dzyaloshinskii-Moriya interaction (DMI), appears [17–22]. While the RKKY interaction favors linear alignment of magnetic moments, the DMI is a chiral interaction that promotes orthogonal alignment of the adjacent magnetic moments. The interfacial DMI, mediated by nonmagnetic atoms with strong spin-orbit coupling, has recently been found to induce various intriguing chiral phenomena, such as magnetic skyrmions and chiral magnetic domain walls [23–26]. Recently, both theoretical and experimental studies have revealed the existence of an additional DMI in SAF systems, which links the two magnetic subsystems through an intermediate nonmagnetic layer [27–33]. This particular DMI is referred to as interlayer DMI and has been observed in SAFs with different structures and materials. It has been demonstrated that the interlayer DMI can break the lateral mirror symmetry, enabling field-free spin-orbit torque switching in perpendicular magnetic anisotropy (PMA) SAF [33]. However, the dynamic response of SAFs with interlayer DMI, an important parameter for applications, remains unexplored, highlighting the need for a systematic investigation.

On the other hand, recent studies on dynamic responses of magnon-magnon hybrid systems have revealed the coupling between two different magnon modes [34–45]. In comparison to the extensively studied magnon-photon coupling [46–49], magnon-magnon coupling typically exhibits a stronger coupling strength $g/2\pi$, owing to the substantial overlap in the spatial distributions of the two modes. Consequently, magnon-magnon hybrid systems have great potential in quantum engineering [50]. In order to enhance the efficiency of quantum information processing, enhancing the value of $g/2\pi$ is a key objective in research. Generally, $g/2\pi$ can be categorized into several regimes. When $g/2\pi$ is smaller than the loss $\kappa/2\pi$ (the half-width at half-maximum linewidth of resonance peak), the system is in the weak coupling regime, wherein the system energy is dissipated before the energy transfer between the two modes is complete. On the other

*These authors contributed equally to this work.
†Corresponding author: xfhan@iphy.ac.cn
‡Corresponding author: guoqiangyu@iphy.ac.cn

hand, once $g/2\pi$ exceeds $\kappa/2\pi$, the system enters the strong coupling regime, whereby the aforementioned energy transfer can be accomplished. When $g/2\pi$ becomes comparable to the center frequency of the system $\omega_0/2\pi$, i.e., $g > 0.1\omega_0$, the ultrastrong coupling (USC) regime is achieved. In this regime, the rotating-wave approximation is no longer applicable, resulting in many novel phenomena, such as nontrivial ground state, virtual excitations, and higher-order processes. Some of these phenomena are still awaiting exploration [51,52]. Therefore, achieving the USC regime is currently a prominent research focus. While strong magnon-magnon coupling has been achieved in various structures, the USC is rarely reported and is primarily observed in bulk materials [42,43]. Hence, investigating the feasibility of on-chip USC is of significant importance. Considering that SAFs are highly tunable and compatible with the complementary metal-oxide-semiconductor platform, we note that SAFs are such ideal systems. Another key objective in coupling research is to explore the underlying mechanisms. MacNeill *et al.* [36] have demonstrated that a rotation-symmetry breaking is required to induce coupling, as the exchange interaction alone cannot break the symmetry. In order to break the symmetry in SAFs, several strategies have been employed, including the application of an oblique dc magnetic field out of the sample plane [39], the introduction of a dynamic dipolar interaction [38], and the introduction of magnetic moments asymmetry between the two ferromagnetic layers (FMs) [41,45]. In light of the chiral nature of the interlayer DMI, we point out that this recently discovered interaction can also be utilized to break the symmetry. Although very recently the DMI-induced magnon-magnon coupling has been observed in hybrid perovskite antiferromagnets [53], the high tunability of SAFs suggests the potential for achieving stronger coupling and even entering the USC regime in SAF systems by utilizing the interlayer DMI. Therefore, a systematic investigation is necessary to explore this possibility.

Here, we investigate the dynamic response of SAFs with interlayer DMI through theoretical analysis and micromagnetic simulations, and reveal the presence of strong and ultrastrong magnon-magnon coupling in this system. By conducting symmetry analysis, we demonstrate that the interlayer DMI breaks (protects) the rotation symmetry in both PMA SAF and in-plane magnetic anisotropy (IP) SAF when the interlayer DMI vector $\mathbf{D}$ is nonorthogonal (orthogonal) to the external dc magnetic field, resulting in the emergence (vanishing) of the magnon-magnon coupling. $g/2\pi$ is extracted accurately by using the generalized Hopfield model. We highlight that $g/2\pi$ can be tuned from the weak coupling regime to the strong coupling and even ultrastrong coupling regimes by manipulating the orientation of $\mathbf{D}$, the magnetic anisotropy field, the interlayer DMI intensity, and the RKKY interaction intensity. Interestingly, we observe a significant enhancement in the coupling strength when the total magnetic anisotropy field approaches zero, i.e., interface anisotropy and magnetic crystal anisotropy almost compensating for shape anisotropy. In this case, the normalized coupling strength g/ω_0 can reach about 0.5, even with a relatively small interlayer DMI. Such a large g/ω_0 indicates that the system is deep into the USC regime. Additionally, we discover that the coupling properties exhibit remarkable sensitivity to the magnetic anisotropy field, as even a minor change in the magnetic anisotropy field ($\sim$100 Oe) can lead to a substantial variation in g/ω_0 ($\sim$0.4). Our findings uncover fascinating magnon-magnon coupling properties in SAFs with interlayer DMI and present a pathway towards USC in magnon-magnon hybrid systems, which has considerable implications for the experimental research.

II. SYMMETRY DESCRIPTION OF SAFS WITH INTERLAYER DMI

The structure of a SAF with interlayer DMI is depicted in Fig. 1(a). It consists of a nonmagnetic layer (NM) sandwiched between two ferromagnetic layers (FM1 and FM2). Two types of interactions are considered in the system: the collinear RKKY interaction represented by the orange arrows, and the chiral interlayer DMI represented by the violet arrows. When a small radio-frequency magnetic field is applied, the magnetic moment unit vectors $\mathbf{m_1}$ and $\mathbf{m}_2$ start to undergo precession around their stationary positions $\mathbf{m_1^{eq}}$ and $\mathbf{m_2^{eq}}$, respectively. By satisfying specific frequency conditions, the precession angles can be significantly amplified, leading to resonance. To modulate the dynamic response of the system, an external dc magnetic field $\mathbf{H}$ is applied in the SAF plane. For convenience, a global Cartesian coordinate system is introduced, where $\mathbf{e_x} = \mathbf{H}/H$, $\mathbf{e_z} = \mathbf{n}$, and $\mathbf{e_y} = \mathbf{e_z} \times \mathbf{e_x}$. Here, $\mathbf{n}$ represents the unit vector perpendicular to the SAF plane, and H denotes the magnitude of the external dc magnetic field. The violet solid arrow indicates the interlayer DMI vector $\mathbf{D}$, which lies in the x-y plane at an angle of ψ with respect to the x axis.

In this section, we will explore the impact of interlayer DMI on the symmetry of SAFs. A macrospin model is established. The total energy per unit area of such a SAF can be expressed as

$$E = E_{\text{Zeeman}} + E_{\text{Ani}} + E_{\text{RKKY}} + E_{\text{DMI}}, \tag{1}$$

with

$$E_{\text{Zeeman}} = -\mu_0 d_1 M_{S1} \mathbf{m_1} \cdot \mathbf{H} - \mu_0 d_2 M_{S2} \mathbf{m_2} \cdot \mathbf{H}$$

$$E_{\text{Ani}} = -\tfrac{1}{2}\mu_0 H_{k1} M_{S1} d_1 (\mathbf{m_1} \cdot \mathbf{e_z})^2 - \tfrac{1}{2}\mu_0 H_{k2} M_{S2} d_2 (\mathbf{m_2} \cdot \mathbf{e_z})^2$$

$$E_{\text{RKKY}} = -J(\mathbf{m_1} \cdot \mathbf{m_2})$$

$$E_{\text{DMI}} = -\mathbf{D} \cdot (\mathbf{m_1} \times \mathbf{m_2}).$$

The E_{Zeeman} term corresponds to the Zeeman energy. The E_{Ani} term corresponds to the anisotropy energy, where we specifically consider the z-axis magnetic anisotropy in each FM while neglecting the in-plane uniaxial magnetic anisotropy. The E_{RKKY} term corresponds to the RKKY interaction energy. And, the E_{DMI} term corresponds to the interlayer DMI energy. Here, μ_0 represents the permeability of vacuum. d_i, M_{Si}, and H_{ki} ($i = 1, 2$) are the thickness, saturation magnetization, and total magnetic anisotropy field of each FM, respectively. $H_{ki} > 0$ indicates perpendicular magnetic anisotropy, while $H_{ki} < 0$ indicates easy-plane magnetic anisotropy. J is the RKKY exchange constant, which is negative due to antiferromagnetic coupling. $\mathbf{D} = D\mathbf{e_D}$ is the interlayer DMI vector as mentioned above. Here, D denotes the magnitude of interlayer DMI, and $\mathbf{e_D}$ is a unit vector that indicates the direction of interlayer DMI. The stationary

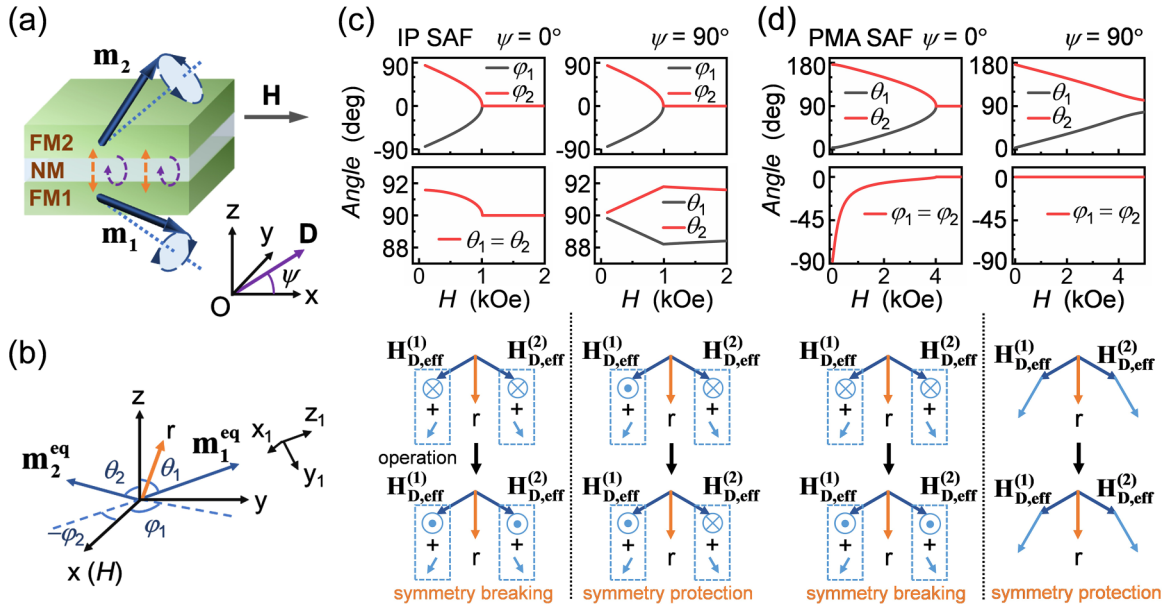

FIG. 1. (a) Schematic diagram of resonance in a SAF structure with interlayer DMI. Two ferromagnetic layers are separated with a nonmagnetic spacer. The external magnetic field **H** is applied along the x axis. In each FM, the blue dashed line and the circle indicate the stationary direction and precession trajectory of the magnetic moment, respectively. Orange and violet arrows (dashed) represent the colinear RKKY interaction and chiral interlayer DMI, respectively. The interlayer DMI vector **D**, represented by the violet arrow, lies in the x-y plane with an angle of ψ to the x axis. (b) The coordinate systems used in our SAF system. Two coordinate systems are used in this study: the global coordinate system x-y-z and the local coordinate system x_1-y_1-z_1. (c), (d) The equilibrium polar angles and azimuth angles of $\mathbf{m_1}$ and $\mathbf{m_2}$ in a typical IP SAF (c) and a typical PMA SAF (d) when ψ equals 0° and 90°, respectively. The parameters for the IP SAF are $H_k = -8$ kOe, $H_{ex} = -0.5$ kOe, and $H_D = 0.25$ kOe. The parameters for the PMA SAF are $H_k = 3$ kOe, $H_{ex} = -0.5$ kOe, and $H_D = 0.25$ kOe. The diagrams of the m-O-r plane illustrate the mechanisms by which symmetry is protected or broken under different conditions. The dark blue and orange arrows represent the stationary magnetic moments and the r axis, respectively. The light blue arrows inside each box correspond to the two directional components of the effective interlayer DMI field $\mathbf{H}^{(i)}_{D,eff}$ acting on FM$_i$. One component is perpendicular to the m-O-r plane, and the other is in the m-O-r plane.

positions and dynamic responses of $\mathbf{m_1}$ and $\mathbf{m_2}$ are governed by the Landau-Lifshitz-Gilbert equations:

$$\frac{d\mathbf{m_1}}{dt} = -\gamma \mathbf{m_1} \times \mathbf{H_{eff1}} + \alpha_1 \mathbf{m_1} \times \frac{d\mathbf{m_1}}{dt}$$
$$\frac{d\mathbf{m_2}}{dt} = -\gamma \mathbf{m_2} \times \mathbf{H_{eff2}} + \alpha_2 \mathbf{m_2} \times \frac{d\mathbf{m_2}}{dt}, \quad (2)$$

where the gyromagnetic ratio γ is set to 2.8 GHz/kOe. α_1 and α_2 denote the Gilbert damping constants of FM1 and FM2, respectively. In our theoretical part, we simplify the model by neglecting α_1 and α_2. $\mathbf{H_{eff1}}$ and $\mathbf{H_{eff2}}$ correspond to the effective magnetic fields in FM1 and FM2, respectively:

$$\mathbf{H_{eff1}} = \mathbf{H} + H_{k1}(\mathbf{m_1} \cdot \mathbf{e_z})\mathbf{e_z} + H_{ex}\mathbf{m_2} + H_D \mathbf{m_2} \times \mathbf{e_D}$$
$$\mathbf{H_{eff2}} = \mathbf{H} + H_{k2}(\mathbf{m_2} \cdot \mathbf{e_z})\mathbf{e_z} + \lambda H_{ex}\mathbf{m_1} + \lambda H_D \mathbf{e_D} \times \mathbf{m_1}, \quad (3)$$

where $H_{ex} = J/(\mu_0 M_{S1} d_1)$ corresponds to the effective RKKY exchange field acting on FM1. $H_D = D/(\mu_0 M_{S1} d_1)$ corresponds to the effective interlayer DMI field acting on FM1 when $\mathbf{m_2}$ is perpendicular to $\mathbf{e_D}$. $\lambda = (M_{S1} d_1)/(M_{S2} d_2)$ denotes the ratio of the two magnetic moments.

For an $\mathbf{m_i}$ excited at a certain frequency $\omega = 2\pi f$, it can be divided into two components: an equilibrium component $\mathbf{m_i^{eq}}$ and a rapidly oscillating component $\delta\mathbf{m_i}e^{i\omega t}$. We begin by solving for the equilibrium positions by setting $d\mathbf{m_i}/dt$ in Eq. (2) to zero. As depicted in Fig. 1(b), we utilize the polar angle θ_i and azimuth angle φ_i to indicate the position of $\mathbf{m_i^{eq}}$. To account for the symmetry, we introduce an r axis: $\mathbf{e_r} || \mathbf{m_1^{eq}} + \mathbf{m_2^{eq}}$, as indicated by the orange arrow. The r axis and the two $\mathbf{m_i^{eq}}$ lie in a plane labeled m-O-r. Here, to minimize the influence of other asymmetrical factors, we set $H_{k1} = H_{k2} = H_k$ and $\lambda = 1$. The PMA SAF tends to be magnetized perpendicular to the plane when $H = 0$ and $H_k > 0$. Conversely, magnetic moments of the IP SAF tend to lie in plane when $H = 0$ and $H_k < 0$. We first consider a traditional SAF without interlayer DMI, i.e., $D = 0$. In this case, for an IP SAF, $\mathbf{m_i^{eq}}$ is in the x-y plane when **H** is applied, i.e., $\theta_1 = \theta_2 = 90°$. And, φ_i has an analytical solution: $\varphi_2 = -\varphi_1 = \arccos(H/-2H_{ex})$, assuming the total magnetic moment is unsaturated and φ_2 is taken as positive. Similarly, for a PMA SAF, $\mathbf{m_i^{eq}}$ is in the x-z plane when **H** is applied, i.e., $\varphi_1 = \varphi_2 = 0°$. And, $\theta_1 = 180° - \theta_2 = \arcsin[H/(H_k - 2H_{ex})]$, when the total magnetic moment is unsaturated. Therefore, the r axis coincides with the x axis in these two cases. We introduce a rotating operator C_{2r} which performs a 180° rotation about the r axis. Under the combined operation of C_{2r} and sublattice exchange, the system exhibits symmetry due to the symmetric $\mathbf{H_{effi}}$ when $D = 0$. Consequently, no coupling phenomenon is observed in this case [36]. However, when taking into account the interlayer DMI, we emphasize that the introduced effective interlayer DMI fields $\mathbf{H^{(1)}_{D,eff}} = H_D \mathbf{m_2} \times \mathbf{e_D}$ and $\mathbf{H^{(2)}_{D,eff}} =$

$H_D \mathbf{e_D} \times \mathbf{m_1}$ can break the symmetry of the system. Figure 1(c) displays θ_i and φ_i of a typical IP SAF with interlayer DMI, where two cases are considered: $\psi = 0^\circ$ and $\psi = 90^\circ$. When $\psi = 0^\circ$, φ_2 and θ_2 are equal to $-\varphi_1$ and θ_1, respectively. We note that in this case, due to the chirality of the interlayer DMI, $\mathbf{H}^{(1)}_{\mathbf{D,eff}}$ and $\mathbf{H}^{(2)}_{\mathbf{D,eff}}$ are predominantly perpendicular to the *m-O-r* plane with the same direction. Thus, under the combined operation, the direction of the two perpendicular components is reversed, resulting in the breaking of the system's symmetry, as shown in the bottom panel of Fig. 1(c). In addition to the perpendicular components, there is a minor component of $\mathbf{H}^{(i)}_{\mathbf{D,eff}}$ that lies in the *m-O-r* plane. This occurs because θ_i is no longer equal to 90°, resulting in a slight misalignment between the *m-O-r* plane and the *x-y* plane. Analysis shows that these minor components in two FMs remain unchanged under the combined operation. On the other hand, when $\psi = 90^\circ$, φ_2 and θ_2 are equal to $-\varphi_1$ and $180^\circ - \theta_1$, respectively. In this case, however, the perpendicular components of $\mathbf{H}^{(1)}_{\mathbf{D,eff}}$ and $\mathbf{H}^{(2)}_{\mathbf{D,eff}}$ have opposite directions. Thus, under the combined operation, the directions of the two perpendicular components remain unchanged. Besides, the minor component of $\mathbf{H}^{(i)}_{\mathbf{D,eff}}$ in the *m-O-r* plane is similar to the case of $\psi = 0^\circ$. Therefore, symmetry is protected under the combined operation when $\psi = 90^\circ$. The PMA SAF example is shown in Fig. 1(d). Through a similar analysis, we show that the system's symmetry is also broken (protected) when $\psi = 0^\circ$ ($\psi = 90^\circ$). Additionally, when $\psi = 90^\circ$, we note that the total magnetic moment remains unsaturated even at a relatively large H. This characteristic can give rise to blueshifts in the resonance frequencies, which will be elucidated later.

The above analysis of symmetry suggests that the magnon-magnon coupling can be tuned by manipulating ψ. To demonstrate this, we calculate the dynamic responses of the SAFs. In order to decouple the two equations in Eq. (2) when the system is symmetric, two joint precession vectors are defined: $\delta\mathbf{m}_+ = \delta\mathbf{m_1} + C_{2r}\delta\mathbf{m_2}$ and $\delta\mathbf{m}_- = \delta\mathbf{m_1} - C_{2r}\delta\mathbf{m_2}$, corresponding to the pure optical and pure acoustic modes, respectively. For convenience, a local coordinate system is introduced: $\mathbf{e_{z1}} || \mathbf{m}^{\mathbf{eq}}_{\mathbf{1}}$, $\mathbf{e_{x1}} \perp \mathbf{e_{z1}}$, and $\mathbf{e_{y1}} = \mathbf{e_{z1}} \times \mathbf{e_{x1}}$, as shown in Fig. 1(b), where $\mathbf{e_{x1}}$ is parallel to the *x-y* plane. The *r* axis is characterized by the polar angle θ_r and azimuth angle φ_r in this local coordinate system. Subsequently, we project $\delta\mathbf{m}_+$ and $\delta\mathbf{m}_-$ onto the local coordinate system: $\delta\mathbf{m}_+ = \delta m_{+,x1}\mathbf{e_{x1}} + \delta m_{+,y1}\mathbf{e_{y1}}$, $\delta\mathbf{m}_- = \delta m_{-,x1}\mathbf{e_{x1}} + \delta m_{-,y1}\mathbf{e_{y1}}$. Finally, Eq. (2) can be expressed in the following form:

$$i\frac{\omega}{\gamma}\begin{bmatrix}\delta m_{+,x1}\\ \delta m_{+,y1}\\ \delta m_{-,x1}\\ \delta m_{-,y1}\end{bmatrix} = \begin{bmatrix}A_{11} & A_{12} & A_{13} & A_{14}\\ A_{21} & A_{22} & A_{23} & A_{24}\\ A_{31} & A_{32} & A_{33} & A_{34}\\ A_{41} & A_{42} & A_{43} & A_{44}\end{bmatrix}\begin{bmatrix}\delta m_{+,x1}\\ \delta m_{+,y1}\\ \delta m_{-,x1}\\ \delta m_{-,y1}\end{bmatrix}. \quad (4)$$

Due to the spatial distribution characteristics of $\mathbf{m}^{\mathbf{eq}}_{\mathbf{i}}$ when $D \neq 0$, the matrix elements A_{nm} become quite complex and they are presented in the Supplemental Material [54]. By solving the secular equation of Eq. (4), the resonance frequency f_{res} can be obtained. Since the angles θ_i and φ_i cannot be solved analytically at arbitrary angles, f_{res} is calculated numerically. However, if we consider only the first-order approximation of θ_i and φ_i, we can solve f_{res} analytically with relatively high accuracy, which will be mentioned later.

We start by considering the IP SAF case. As depicted in Fig. 2(a), the resonance spectra of the typical IP SAF are calculated for $\psi = 0^\circ$ and 90°. It can be seen that two branches appear in each panel. We label the high-frequency branch as "I" and the low frequency branch as "II." Previous studies on SAFs without interlayer DMI have demonstrated that there is no coupling between the optical and acoustic modes when H is in plane [36,39], resulting in the absence of gap between the two branches. However, in Fig. 2(a), when $\psi = 0^\circ$, a gap is clearly visible, indicating the occurrence of magnon-magnon coupling. The dashed curves represent the pure optical and acoustic modes, which intersect at $H = H_0$ with a frequency of $\omega_0/2\pi$. The value $\omega_0/2\pi$ is the center frequency, which corresponds to the basic energy level of the system in the absence of magnon-magnon coupling. On the contrary, the gap vanishes when $\psi = 90^\circ$, indicating a decoupling of the optical and acoustic modes. In this case, branch I and branch II coincide with the acoustic and optical modes. Therefore, we point out that the coupling characteristics are consistent with the symmetry analysis illustrated in Fig. 1. While previous studies approximate the coupling strength $g/2\pi$ by half of the minimum of the gap, we emphasize that this approach holds true only when $g/2\pi$ is not large. To accurately extract $g/2\pi$, we quantize our system using a generalized Hopfield model, wherein the Hamiltonian can be expressed as

$$\hat{\mathcal{H}} = \hbar\omega_+\left(\hat{a}^\dagger_+\hat{a}_+ + \tfrac{1}{2}\right) + \hbar\omega_-\left(\hat{a}^\dagger_-\hat{a}_- + \tfrac{1}{2}\right) + i\hbar g_1(\hat{a}_+\hat{a}^\dagger_- - \hat{a}^\dagger_+\hat{a}_-) + i\hbar g_2(\hat{a}^\dagger_+\hat{a}^\dagger_- - \hat{a}_+\hat{a}_-). \quad (5)$$

Here, ω_+ and ω_- are the frequencies of the pure optical and acoustic modes, respectively. g_1 and g_2 are the corotating coupling strength and counter-rotating coupling strength, respectively. The expressions for these quantities are provided in Supplemental Material [54]. $\hat{a}_+$ ($\hat{a}_-$) and $\hat{a}^\dagger_+$ ($\hat{a}^\dagger_-$) correspond to the annihilation and creation operators of the optical (acoustic) mode magnon, respectively. $\hbar$ is the reduced Planck constant. We calculate g_1 and g_2 at $H = H_0$. The results demonstrate that, unlike most traditional coupling systems such as superconducting circuits and semiconductor quantum wells where g_2 is generally equal to g_1 [55–57], in our IP SAF system, $g_2(H_0)$ is slightly smaller than $g_1(H_0)$. Since the gap is primarily induced by the corotating term when $g_2(H_0)$ is not sufficiently large, we only consider $g_1(H_0)$ in the main text. For simplicity, we refer to $g_1(H_0)$ as g. The results of $g_2(H_0)$ are presented in Supplemental Material [54]. Additionally, in the above discussion, we only consider two specific ψ's, 0° and 90°. To further illustrate the tunability of the coupling strength, we depict $g/2\pi$ as a function of ψ in Fig. 2(b). As can be seen, the function exhibits a horizontal "8" shape. We note that it possesses two axes of symmetry, as shown by the orange dashed lines. This indicates that for a given $\psi = \psi_0$, the following four cases are equivalent: $\psi = \psi_0$, $-\psi_0$, $180^\circ - \psi_0$, and $180^\circ + \psi_0$. The curve represents the approximate analytical solutions, consistent with the numerical solutions denoted by the circles. We note that in this typical IP SAF, the maximum value of $g/2\pi$ is obtained at $\psi = 0^\circ$, which exceeds 0.4 GHz. As ψ increases from 0° to 90°, $g/2\pi$ decreases monotonically until it reaches zero. To

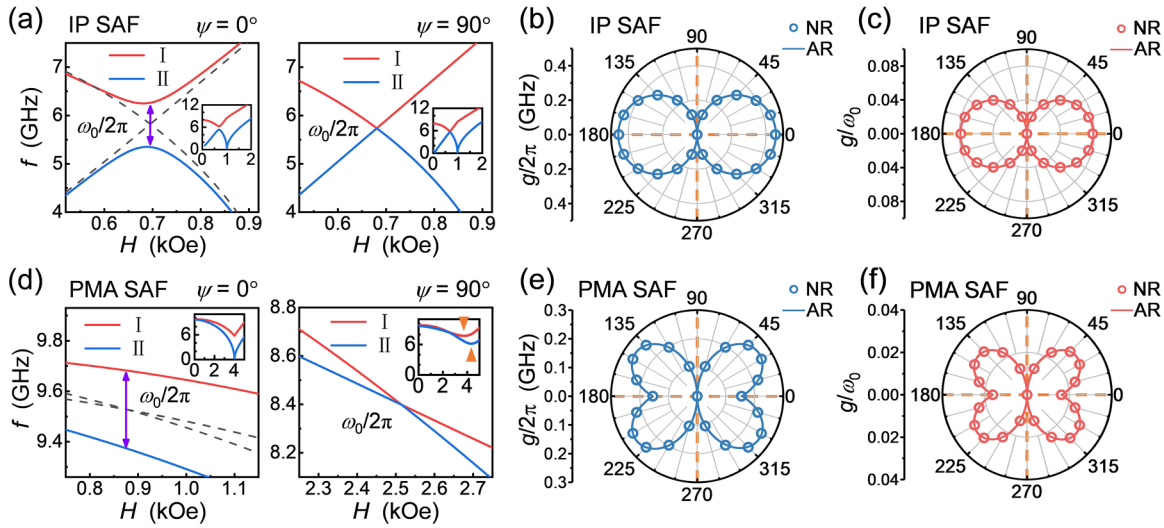

FIG. 2. (a)–(c) Magnon-magnon coupling characteristics in the IP SAF structure illustrated in Fig. 1(c). (a) Presents resonance spectra for $\psi = 0^\circ$ and 90°. The red and blue curves represent the high-frequency branches (I) and the low-frequency branches (II), respectively. The dashed curves represent the pure optical mode and the acoustic mode. A gap marked with a violet arrow is shown between the frequency branches when $\psi = 0^\circ$. No gap is seen when $\psi = 90^\circ$, because the spectral curves coincide with those of pure optical and acoustic modes. $\omega_0/2\pi$ is the center frequency for each case. Insets represent the full-range spectra, where the units of horizontal and vertical coordinates are the same as in the main plots. (b) and (c) present the coupling strength $g/2\pi$ and the normalized coupling strength g/ω_0 as functions of ψ, respectively. Numerical results (NR) are visualized with circles, and analytical results (AR) are shown by solid curves where we consider the first-order approximation of $\theta_{1(2)}$ and $\varphi_{1(2)}$. The orange dashed lines represent the axes of symmetry. (d)–(f) Magnon-magnon coupling characteristics in the PMA SAF structure illustrated in Fig. 1(d). Similarly, (d) presents the resonance spectra for $\psi = 0^\circ$ and 90°. (e) and (f) show $g/2\pi$ and g/ω_0 as a function of ψ, respectively. Orange arrows mark frequency blueshifts of PMA SAF in the inset of (d).

compare g with the system energy, the normalized coupling strength is introduced, which is defined as the ratio of coupling strength to the center frequency g/ω_0. Figure 2(c) illustrates the calculated g/ω_0 as a function of ψ. It should be noted that ω_0 is also a function of ψ; thus, the shape of the g/ω_0-ψ curve is not exactly the same as the $g/2\pi$-ψ curve. The maximum g/ω_0 is also obtained at $\psi = 0^\circ$, approximately 0.08, which is close to the lower bound for the USC regime.

Next, we consider the PMA SAF case. As depicted in Fig. 2(d), the resonance spectra of the typical PMA SAF are also calculated for $\psi = 0^\circ$ and 90°. Similarly, a gap emerges when $\psi = 0^\circ$, and vanishes when $\psi = 90^\circ$. However, in the PMA SAF case, there are large changes in the center frequency ω_0 and the corresponding magnetic field H_0 as ψ increases from 0° to 90°. The full spectra in the insets also indicate that the PMA SAF system is extremely different from the IP SAF system. One of the most striking features of PMA SAF is that the spectrum can be greatly modified by the interlayer DMI when $\psi = 90^\circ$. We use orange arrows to label the minimum frequencies of branch I and branch II. Compared with the $\psi = 0^\circ$ case, these frequencies show large blueshifts, which originate from the unsaturated magnetic moments as mentioned in Fig. 1(d). We point out that these blueshifts are tunable with ψ and reach their maximum values at $\psi = 90^\circ$, as shown in Supplemental Material [54]. The analysis of $g_1(H_0)$ and $g_2(H_0)$ shows that $g_2(H_0)$ is much smaller than $g_1(H_0)$ in the PMA SAF case. Therefore, we adopt the same approach as in the IP SAF case. Figure 2(e) shows $g/2\pi$ as a function of ψ for the PMA SAF case. Unlike Fig. 2(b), this function exhibits a butterfly-like shape. However, the symmetry of the function is consistent with the IP SAF case, and the analytical solutions also agree well with the numerical solutions. The maximum $g/2\pi$ is smaller than that of the IP SAF case, and is no longer obtained at $\psi = 0^\circ$. As ψ increases from 0° to 90°, $g/2\pi$ first increases and then decreases to zero. We also calculate g/ω_0 in Fig. 2(f), where the maximum value is significantly below 0.1. Additional cases of IP SAFs and PMA SAFs are presented in Supplemental Material [54], where we demonstrate that the analytical solutions remain valid even with further increase in H_D. However, the analytical solutions become inappropriate as H_k approaches zero. This also implies that when H_k approaches zero, the system exhibits interesting coupling properties that will be discussed in the next section.

III. REALIZATION OF THE USC IN SAFS WITH INTERLAYER DMI

The aforementioned results demonstrate the feasibility of USC induced by interlayer DMI. To fully comprehend the impact of various parameters on the coupling properties, we set ψ to 0° and construct color plots of $g/2\pi$ and g/ω_0 in Fig. 3. We first fix H_{ex} at -0.5 kOe and calculate $g/2\pi$ and g/ω_0 as functions of H_k and the ratio of interlayer DMI to RKKY interaction $D/|J|$, as shown in Figs. 3(a) and 3(b), respectively. It can be seen that $g/2\pi$ and g/ω_0 increase monotonically with the increase of $D/|J|$ when H_k is held at an arbitrary value. However, $g/2\pi$ and g/ω_0 as functions of H_k are relatively intricate when $D/|J|$ is fixed. We divide the color plot into two regions: the PMA SAF region ($H_k > 0$) and the IP SAF region ($H_k < 0$). In Fig. 3(a), $g/2\pi$ decreases as $|H_k|$ decreases within the IP SAF region, while it increases

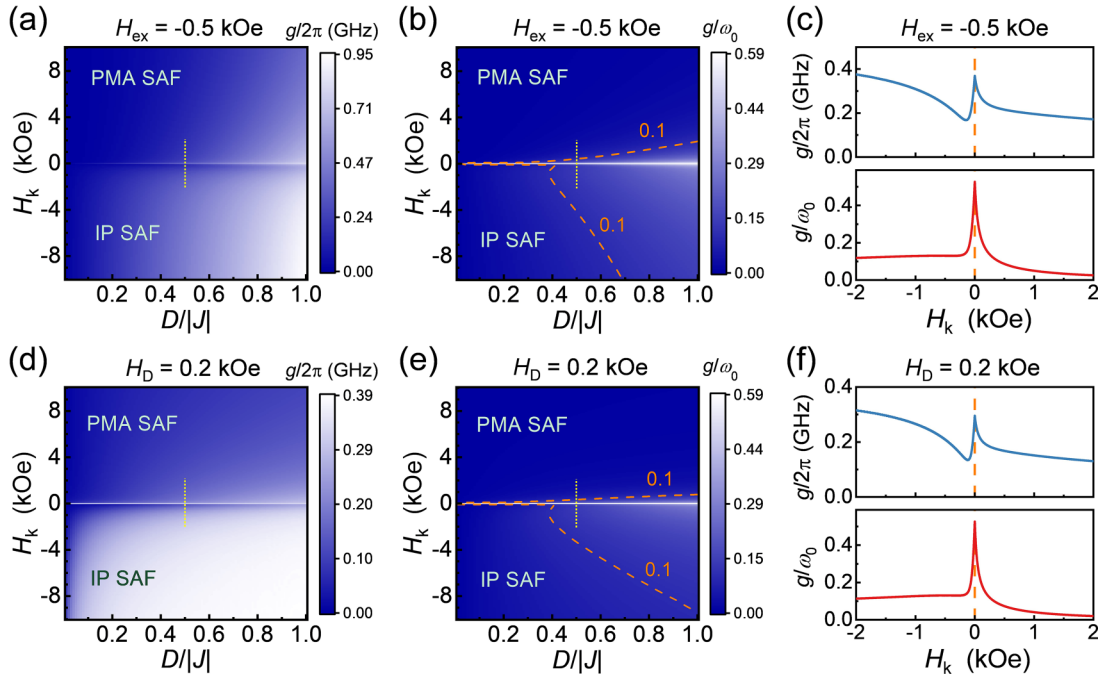

FIG. 3. (a), (b) Color plots of $g/2\pi$ (a) and g/ω_0 (b) as functions of the magnetic anisotropy field H_k and the ratio $D/|J|$ when H_{ex} and ψ are fixed at -0.5 kOe and 0°, respectively. (d), (e) Color plots of $g/2\pi$ (d) and g/ω_0 (e) as functions of the magnetic anisotropy field H_k and the ratio $D/|J|$ when H_D and ψ are fixed at 0.2 kOe and 0°, respectively. Dashed curves in (b) and (e) mark the lower bound for the USC regime, $g/\omega_0 = 0.1$. The values of $g/2\pi$ and g/ω_0 feature an abrupt jump when H_k approaches zero. (c) and (f) represent the corresponding curves plotted along dashed yellow segments set at $D/|J| = 0.5$ in (a), (b), (d), and (e). The orange dashed lines represent $H_k = 0$.

as $|H_k|$ decreases within the PMA SAF region. However, near the boundary of the IP SAF region, a sudden increase in $g/2\pi$ is observed. A close-up is shown by the blue curve in Fig. 3(c). Clearly, when $H_k = 0$, $g/2\pi$ reaches a local maximum, which is an intriguing boundary phenomenon. In Fig. 3(b), within both the PMA SAF region and IP SAF region, g/ω_0 increases as $|H_k|$ decreases. When H_k approaches zero, a sudden increase in g/ω_0 is also observed. Interestingly, the increase in g/ω_0 is more pronounced than the increase in $g/2\pi$ due to the decrease in ω_0 near the boundary. The corresponding close-up is shown by the red curve in Fig. 3(c). We note that a peak is clearly visible at $H_k = 0$. The maximum g/ω_0 even surpasses 0.5, indicating that the system is able to be deep into the USC regime. To determine the conditions for USC realization, we plot the lower bound for the USC regime, as shown by the dashed curves in Fig. 3(b). It can be seen that the USC regime is easier to achieve in the IP SAF region. Particularly, when H_k approaches zero, the USC regime can be realized even at very low values of $D/|J|$. For example, with $H_k = -0.1$ Oe, $D/|J|$ only needs to be 0.02 ($H_D = 10$ Oe) to satisfy the USC requirement. It is worth noting that such a small H_D can be easily achieved in experiments, as experimental H_D have reached the order of 100 Oe or even several hundred Oe [30,32]. The above discussions are based on a fixed H_{ex}. To investigate the effect of H_{ex} on the coupling, we subsequently fix H_D at 0.2 kOe and calculate $g/2\pi$ and g/ω_0 as functions of H_k and $D/|J|$, as shown in Figs. 3(d) and 3(e), respectively. We note that these two plots exhibit similar characteristics to Figs. 3(a) and 3(b): both $g/2\pi$ and g/ω_0 increase monotonically with the increase of $D/|J|$ when H_k is held constant, and the plots of g/ω_0 feature the same peak when H_k approaches zero, as shown in Fig. 3(f). These results indicate that in the vicinity of the boundary between the two regions, the enhancement of $g/2\pi$ and g/ω_0 is a general property. This enhancement can be explained from a physical perspective as well: when the interface anisotropy and magnetic crystal anisotropy nearly compensate for the shape anisotropy in both FMs, the anisotropy energy E_{Ani}, which does not contribute to the coupling in our system, is essentially eliminated. Consequently, in this case, the interlayer DMI, which determines the degree of the system's asymmetry, can play its role to the greatest extent.

In order to investigate the coupling properties when H_k approaches zero in more detail, we study the coupling properties as functions of ψ at three selected typical H_k values: -100, -1, and 100 Oe. In this part, H_{ex} and H_D are set to moderate values: -0.5 and 0.2 kOe, respectively. To simulate the experiments, we perform micromagnetic simulations as well, which are carried out using the open-source OOMMF. In the micromagnetic simulations, each FM in a SAF has a thickness of 5 nm, a length and width of 300 nm, and is divided into $10 \times 10 \times 1$ grids. The Heisenberg exchange-strength coefficient A, the saturation magnetization intensity M_S, and the Gilbert damping constant α are set at 1×10^{-11} J/m, 1×10^6 A/m, and 0.01, respectively. For comparison with the macrospin model, J and D are set at -2.5×10^{-4} and 1×10^{-4} J/m^2, respectively. The dc magnetic field is applied in the x direction. To extract the dynamic responses, a sinc alternating magnetic field with amplitudes of 0.5 Oe in both the x and y directions is applied. The simulation time step is set at 25 or 100 ps, and the simulation runs for 25, 100, or 250 ns, depending on the specific configuration. At each time

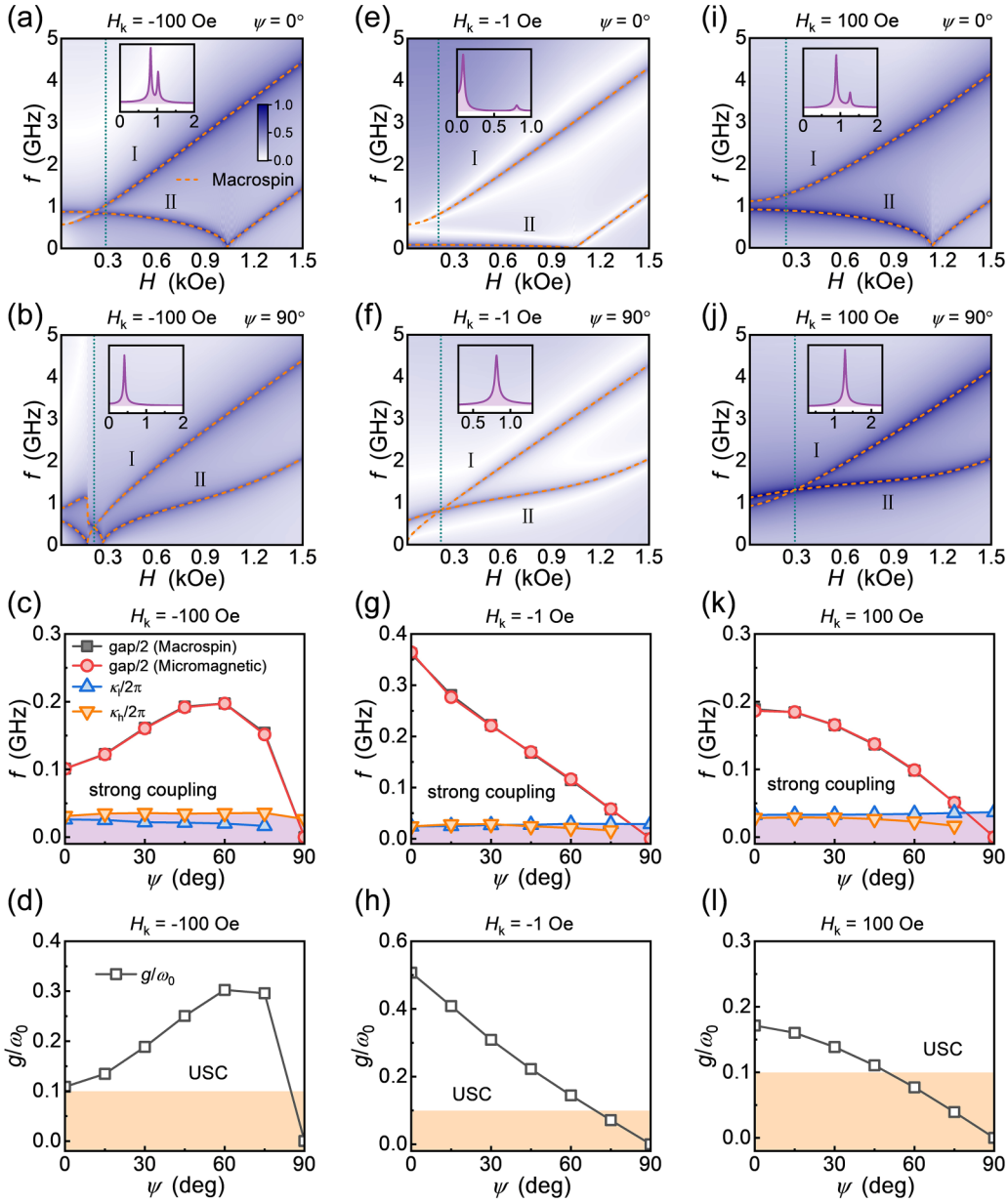

FIG. 4. Magnon-magnon coupling parameters calculated for $H_{ex} = -0.5$ kOe and $H_D = 0.2$ kOe when varying H_k: (a)–(d) −100 Oe; (e)–(h) −1 Oe; and (i)–(l) 100 Oe. Top panels show the spectra as functions of applied field H, obtained with micromagnetic simulations for the particular cases of $\psi = 0^\circ$ (a), (e), and (i), and 90° (b), (f), and (j). The color bar represents the normalized intensity. Orange dashed curves represent the resonance spectra calculated with the macrospin model. Green dotted lines are used to indicate $H = H_0$ ($\omega_+ = \omega_-$). The insets show the spectra obtained along these dashed lines. Note that the frequency ranges for the insets are different in order to show the branches more clearly. The x coordinate corresponds to frequency f, and the y coordinate corresponds to the intensity. (c), (g), and (k) show half-gap values and losses $\kappa_{h(l)}/2\pi$ calculated for different ψ. The gaps are obtained with two methods: macrospin models and micromagnetic simulations (black squares and red circles, correspondingly). Blue and orange triangles represent the losses for branch II and branch I, respectively. Strong coupling cannot be achieved for parameter combinations shaded in light purple at the bottom part of these plots. (d), (h), and (l) present g/ω_0 as a function of ψ. Similarly, USC cannot be achieved for parameter combinations shaded in light orange at the bottom part of these plots.

step, the magnetization intensity distribution is obtained, and the local power spectrum of m_y is calculated pointwise using the Fourier transform analysis [58].

Figures 4(a) to 4(d), Figs. 4(e) to 4(h), and Figs. 4(i) to 4(l) show the results for the cases with $H_k = -100$, -1, and 100 Oe, respectively. Noticeably, the resonance spectra show significant variation with small changes in H_k. We first consider the case with $\psi = 0^\circ$, as shown in Figs. 4(a), 4(e), and 4(i). As H_k increases, the frequency of branch II $\omega_{II}/2\pi$ initially decreases to zero, and then increases when H_k changes the sign. Green dotted lines indicate the cases with $H = H_0$, and the corresponding simulation results are displayed in the insets. As can be seen, two discrete peaks appear in each inset, indicating the realization of strong

coupling. By fitting these peaks with the Lorentz function, we can determine the resonance frequency of branch I (II) $\omega_{I(II)}/2\pi$, as well as the resonance frequency linewidth of the high-frequency branch I (low-frequency branch II) $\kappa_{h(l)}/2\pi$. However, when $\psi = 90^\circ$, as shown in Figs. 4(b), 4(f), and 4(j), only one single peak is present, indicating that the system is either uncoupled or in a weak coupling regime. By decreasing α to 0.001, there is still only one peak (not shown here). Therefore, we assume that the simulated coupling gap is zero. Additionally, a spin-flop feature is observed in Fig. 4(b), while this feature disappears when H_k increases. The orange dashed curves in these color plots represent the calculated eigenfrequencies based on the macrospin model, which are all in good agreement with the micromagnetic simulations. Half of the gap and $\kappa_{h(l)}/2\pi$ as functions of ψ are displayed in Figs. 4(c), 4(g), and 4(k). It should be noted that these functions exhibit the same symmetry as the functions in Figs. 2(b) and 2(e). Therefore, we only display the results with ψ between 0° and 90°. Interestingly, the gap as a function of ψ shows very different trends in different plots. When $H_k = -100$ Oe, the gap first increases and then decreases as ψ increases from 0° to 90°, while the gap decreases monotonically when $H_k = -1$ and 100 Oe. The blue and orange triangles represent the extracted losses $\kappa_l/2\pi$ and $\kappa_h/2\pi$, respectively. The losses at $\psi = 90^\circ$ are obtained from the single peak. As can be seen, in most cases of ψ, half of the gaps are much larger than the losses. Figures 4(d), 4(h), and 4(l) show g/ω_0 as a function of ψ. It should be noted that only when g/ω_0 is small, $g/2\pi$ is approximately equal to half of the gap. Therefore, we only display the theoretical results in these plots. As can be seen, as ψ increases, g/ω_0 exhibits a similar trend to the corresponding change in the gap in each plot. And, the USC regime can be achieved in most cases of ψ. It is worth noting that g/ω_0 is highly sensitive to the changes in H_k, and this sensitivity is related to ψ. To illustrate this, we take two examples: $\psi = 0^\circ$ and 60°. For $\psi = 0^\circ$, g/ω_0 exhibits a significant increase ($\sim$0.4) for a small change in H_k (from -100 to -1 Oe), but it decreases sharply as H_k continues to increase. On the other hand, for $\psi = 60^\circ$, g/ω_0 decreases monotonically with the increase of H_k, and it eventually decreases below 0.1. All of these results show that precise adjustment of H_k near zero enables significant tuning of the coupling properties, allowing the activation or deactivation of the USC.

IV. DISCUSSION

Our theoretical studies elucidate the potential of interlayer DMI in inducing USC, and provide a blueprint for experimental exploration. From an experimental perspective, several metallic materials, including Ir, Pt, and Ru, can be used as potential NMs in SAFs [30,32,33]. However, in order to obtain all benefits predicted by our theory, it is imperative that the FMs exhibit specific characteristics, in particular low damping and tunable PMA. We note that Co/Ni multilayers are exemplary candidates for such FMs [59]. By adjusting the composition and the period of Co/Ni stack, one can finely tune the magnetic anisotropy to obtain the desired H_k [60,61]. Moreover, the voltage-controlled magnetic anisotropy effect makes it possible to manipulate H_k in a single sample [62,63]. A recent study has demonstrated that, through the application of a moderate electric field, the H_k of Co/Ni multilayers can be changed by over 2 kOe [64]. Employing this technique, it becomes feasible to readily manipulate the magnetization configurations of samples to realize the USC as proposed in our theory. In addition, the magnetic moments of FM1 and FM2 need not be identical in actual SAF samples, and our theory above only considers the case of $\lambda = 1$. Prior research [41] has indicated that $\lambda \neq 1$ can also lead to magnon-magnon coupling. We explore the coupling properties in SAF systems with both magnetic moments asymmetry and interlayer DMI, as shown in Supplemental Material [54].

In summary, we study the dynamic responses and coupling properties of SAFs with interlayer DMI using theoretical methods and micromagnetic simulations. Our findings reveal that the interlayer DMI can induce strong and ultrastrong magnon-magnon coupling in these systems. Through symmetry analysis, we point out that the interlayer DMI can break the rotation symmetry unless the interlayer DMI vector **D** is orthogonal to the external dc magnetic field. As a result, the magnon-magnon coupling can be turned by manipulating the direction of **D**. We further explore the coupling properties under various conditions, including different magnetic anisotropy fields, interlayer DMI intensities, and RKKY interaction intensities. The results demonstrate significant tunability in the coupling strengths and normalized coupling strengths, allowing for a transition from weak to strong coupling, and even reaching the USC regime. Interestingly, a sudden increase in coupling strength and normalized coupling strength are observed when the system is at the boundary between PMA SAF and IP SAF. In this case, the USC can be achieved even with an extremely small H_D ($\sim$10 Oe), and the maximum normalized coupling strength exceeds 0.5, indicating that the system is deep into the USC regime. Furthermore, we conduct a detailed investigation of the coupling properties near the boundary region. Our analysis reveals that the coupling properties are highly sensitive to the changes in H_k. Even a small adjustment in H_k can lead to significant tuning of the normalized coupling strength. Our study presents a mechanism for realizing ultrastrong magnon-magnon coupling and contributes to the development of this emerging research area.

ACKNOWLEDGMENTS

This work was supported by financial support from the National Key Research and Development Program of China (Grant No. 2022YFA1402800), the National Natural Science Foundation of China (Grants No. 12274437 and No. 52161160334), the Science Center of the National Science Foundation of China (Grant No. 52088101), and the Beijing Natural Science Foundation (Grant No. Z190009).

[1] M. A. Ruderman and C. Kittel, Indirect exchange coupling of nuclear magnetic moments by conduction electrons, Phys. Rev. **96**, 99 (1954).

[2] R. A. Duine, K.-J. Lee, S. S. P. Parkin, and M. D. Stiles, Synthetic antiferromagnetic spintronics, Nat. Phys. **14**, 217 (2018).

[3] P. Grünberg, R. Schreiber, Y. Pang, M. B. Brodsky, and H. Sowers, Layered magnetic structures: Evidence for antiferromagnetic coupling of Fe layers across Cr interlayers, Phys. Rev. Lett. **57**, 2442 (1986).

[4] J. J. Krebs, P. Lubitz, A. Chaiken, and G. A. Prinz, Magnetic resonance determination of the antiferromagnetic coupling of Fe layers through Cr, Phys. Rev. Lett. **63**, 1645 (1989).

[5] S. S. P. Parkin, N. More, and K. P. Roche, Oscillations in exchange coupling and magnetoresistance in metallic superlattice structures: Co/Ru, Co/Cr, and Fe/Cr, Phys. Rev. Lett. **64**, 2304 (1990).

[6] Y.-C. Lau, D. Betto, K. Rode, J. M. D. Coey, and P. Stamenov, Spin-orbit torque switching without an external field using interlayer exchange coupling, Nat. Nanotechnol. **11**, 758 (2016).

[7] C. Bi, H. Almasi, K. Price, T. Newhouse-Illige, M. Xu, S. R. Allen, X. Fan, and W. Wang, Anomalous spin-orbit torque switching in synthetic antiferromagnets, Phys. Rev. B **95**, 104434 (2017).

[8] G. Y. Shi, C. H. Wan, Y. S. Chang, F. Li, X. J. Zhou, P. X. Zhang, J. W. Cai, X. F. Han, F. Pan, and C. Song, Spin-orbit torque in MgO/CoFeB/Ta/CoFeB/MgO symmetric structure with interlayer antiferromagnetic coupling, Phys. Rev. B **95**, 104435 (2017).

[9] P. X. Zhang, L. Y. Liao, G. Y. Shi, R. Q. Zhang, H. Q. Wu, Y. Y. Wang, F. Pan, and C. Song, Spin-orbit torque in a completely compensated synthetic antiferromagnet, Phys. Rev. B **97**, 214403 (2018).

[10] W. J. Kong, C. H. Wan, X. Wang, B. S. Tao, L. Huang, C. Fang, C. Y. Guo, Y. Guang, M. Irfan, and X. F. Han, Spin–orbit torque switching in a T-type magnetic configuration with current orthogonal to easy axes, Nat. Commun. **10**, 233 (2019).

[11] X. Wang, C. Wan, W. Kong, X. Zhang, Y. Xing, C. Fang, B. Tao, W. Yang, L. Huang, H. Wu, M. Irfan, and X. Han, Field-free programmable spin logics via chirality-reversible spin–orbit torque switching, Adv. Mater. **30**, 1801318 (2018).

[12] X. M. Liu, H. T. Nguyen, J. Ding, M. G. Cottam, and A. O. Adeyeye, Interlayer coupling in $Ni_{80}Fe_{20}/Ru/Ni_{80}Fe_{20}$ multilayer films: Ferromagnetic resonance experiments and theory, Phys. Rev. B **90**, 064428 (2014).

[13] H. J. Waring, N. A. B. Johansson, I. J. Vera-Marun, and T. Thomson, Zero-field optic mode beyond 20 GHz in a synthetic antiferromagnet, Phys. Rev. Appl. **13**, 034035 (2020).

[14] X. Luo, Y. Wang, S. Liu, T. Guo, X. Han, and G. Yu, Unusual spin–orbit torque switching in perpendicular synthetic antiferromagnets with strong interlayer exchange coupling, J. Phys.: Condens. Matter **35**, 264004 (2023).

[15] S.-H. Yang, K.-S. Ryu, and S. Parkin, Domain-wall velocities of up to 750 m s^{-1} driven by exchange-coupling torque in synthetic antiferromagnets, Nat. Nanotechnol. **10**, 221 (2015).

[16] S. Bhatti, R. Sbiaa, A. Hirohata, H. Ohno, S. Fukami, and S. N. Piramanayagam, Spintronics based random access memory: A review, Mater. Today **20**, 530 (2017).

[17] S.-H. Yang, R. Naaman, Y. Paltiel, and S. S. P. Parkin, Chiral spintronics, Nat. Rev. Phys. **3**, 328 (2021).

[18] I. Dzyaloshinsky, A thermodynamic theory of "weak" ferromagnetism of antiferromagnetics, J. Phys. Chem. Solids **4**, 241 (1958).

[19] A. Fert and P. M. Levy, Role of anisotropic exchange interactions in determining the properties of spin-glasses, Phys. Rev. Lett. **44**, 1538 (1980).

[20] A. Crépieux and C. Lacroix, Dzyaloshinsky–Moriya interactions induced by symmetry breaking at a surface, J. Magn. Magn. Mater. **182**, 341 (1998).

[21] H. Wu, J. Nance, S. A. Razavi, D. Lujan, B. Dai, Y. Liu, H. He, B. Cui, D. Wu, K. Wong, K. Sobotkiewich, X. Li, G. P. Carman, and K. L. Wang, Chiral symmetry breaking for deterministic switching of perpendicular magnetization by spin-orbit torque, Nano Lett. **21**, 515 (2021).

[22] X. Luo, X. Wang, J. Wei, W. Yang, M. Zhao, Y. Wang, Y. Wang, W. He, B. He, Z. Zeng, C. Wan, X. Han, and G. Yu, Modulation of spin-orbit torque and large enhancement of perpendicular magnetic anisotropy in $W/Co_{20}Fe_{60}B_{20}/MgO$ by Ir insertion layer, Phys. Rev. Appl. **19**, 034043 (2023).

[23] S. Heinze, K. von Bergmann, M. Menzel, J. Brede, A. Kubetzka, R. Wiesendanger, G. Bihlmayer, and S. Blügel, Spontaneous atomic-scale magnetic skyrmion lattice in two dimensions, Nat. Phys. **7**, 713 (2011).

[24] S. Emori, U. Bauer, S.-M. Ahn, E. Martinez, and G. S. D. Beach, Current-driven dynamics of chiral ferromagnetic domain walls, Nat. Mater. **12**, 611 (2013).

[25] W. Jiang, P. Upadhyaya, W. Zhang, G. Yu, M. B. Jungfleisch, F. Y. Fradin, J. E. Pearson, Y. Tserkovnyak, K. L. Wang, O. Heinonen, S. G. E. te Velthuis, and A. Hoffmann, Blowing magnetic skyrmion bubbles, Science **349**, 283 (2015).

[26] G. Yu, A. Jenkins, X. Ma, S. A. Razavi, C. He, G. Yin, Q. Shao, Q. L. He, H. Wu, W. Li, W. Jiang, X. Han, X. Li, A. C. Bleszynski Jayich, P. K. Amiri, and K. L. Wang, Room-temperature skyrmions in an antiferromagnet-based heterostructure, Nano Lett. **18**, 980 (2018).

[27] A. Fernández-Pacheco, E. Vedmedenko, F. Ummelen, R. Mansell, D. Petit, and R. P. Cowburn, Symmetry-breaking interlayer Dzyaloshinskii–Moriya interactions in synthetic antiferromagnets, Nat. Mater. **18**, 679 (2019).

[28] D.-S. Han, K. Lee, J.-P. Hanke, Y. Mokrousov, K.-W. Kim, W. Yoo, Y. L. W. van Hees, T.-W. Kim, R. Lavrijsen, C.-Y. You, H. J. M. Swagten, M.-H. Jung, and M. Kläui, Long-range chiral exchange interaction in synthetic antiferromagnets, Nat. Mater. **18**, 703 (2019).

[29] E. Y. Vedmedenko, P. Riego, J. A. Arregi, and A. Berger, Interlayer Dzyaloshinskii-Moriya interactions, Phys. Rev. Lett. **122**, 257202 (2019).

[30] C. O. Avci, C.-H. Lambert, G. Sala, and P. Gambardella, Chiral coupling between magnetic layers with orthogonal magnetization, Phys. Rev. Lett. **127**, 167202 (2021).

[31] K. Wang, L. Qian, S.-C. Ying, and G. Xiao, Spin-orbit torque switching of chiral magnetization across a synthetic antiferromagnet, Commun. Phys. **4**, 10 (2021).

[32] H. Masuda, T. Seki, Y. Yamane, R. Modak, K. I. Uchida, J. Ieda, Y.-C. Lau, S. Fukami, and K. Takanashi, Large antisymmetric interlayer exchange coupling enabling perpendicular magnetization switching by an in-plane magnetic field, Phys. Rev. Appl. **17**, 054036 (2022).

[33] W. He, C. Wan, C. Zheng, Y. Wang, X. Wang, T. Ma, Y. Wang, C. Guo, X. Luo, M. E. Stebliy, G. Yu, Y. Liu, A. V. Ognev, A. S. Samardak, and X. Han, Field-free spin–orbit torque switching enabled by the interlayer Dzyaloshinskii–Moriya interaction, Nano Lett. **22**, 6857 (2022).

[34] J. L. Chen, C. P. Liu, T. Liu, Y. Xiao, K. Xia, G. E. W. Bauer, M. Z. Wu, and H. M. Yu, Strong interlayer magnon-magnon

coupling in magnetic metal-insulator hybrid nanostructures, Phys. Rev. Lett. **120**, 217202 (2018).

[35] S. Klingler, V. Amin, S. Geprägs, K. Ganzhorn, H. Maier-Flaig, M. Althammer, H. Huebl, R. Gross, R. D. McMichael, M. D. Stiles, S. T. B. Goennenwein, and M. Weiler, Spin-torque excitation of perpendicular standing spin waves in coupled YIG/Co heterostructures, Phys. Rev. Lett. **120**, 127201 (2018).

[36] D. MacNeill, J. T. Hou, D. R. Klein, P. Zhang, P. Jarillo-Herrero, and L. Liu, Gigahertz frequency antiferromagnetic resonance and strong magnon-magnon coupling in the layered crystal $CrCl_3$, Phys. Rev. Lett. **123**, 047204 (2019).

[37] Y. Li, W. Cao, V. P. Amin, Z. Z. Zhang, J. Gibbons, J. Sklenar, J. Pearson, P. M. Haney, M. D. Stiles, W. E. Bailey, V. Novosad, A. Hoffmann, and W. Zhang, Coherent spin pumping in a strongly coupled magnon-magnon hybrid system, Phys. Rev. Lett. **124**, 117202 (2020).

[38] Y. Shiota, T. Taniguchi, M. Ishibashi, T. Moriyama, and T. Ono, Tunable magnon-magnon coupling mediated by dynamic dipolar interaction in synthetic antiferromagnets, Phys. Rev. Lett. **125**, 017203 (2020).

[39] A. Sud, C. W. Zollitsch, A. Kamimaki, T. Dion, S. Khan, S. Iihama, S. Mizukami, and H. Kurebayashi, Tunable magnon-magnon coupling in synthetic antiferromagnets, Phys. Rev. B **102**, 100403(R) (2020).

[40] C. Dai and F. Ma, Strong magnon–magnon coupling in synthetic antiferromagnets, Appl. Phys. Lett. **118**, 112405 (2021).

[41] M. Li, J. Lu, and W. He, Symmetry breaking induced magnon-magnon coupling in synthetic antiferromagnets, Phys. Rev. B **103**, 064429 (2021).

[42] L. Liensberger, A. Kamra, H. Maier-Flaig, S. Geprägs, A. Erb, S. T. B. Goennenwein, R. Gross, W. Belzig, H. Huebl, and M. Weiler, Exchange-enhanced ultrastrong magnon-magnon coupling in a compensated ferrimagnet, Phys. Rev. Lett. **123**, 117204 (2019).

[43] T. Makihara, K. Hayashida, G. T. Noe Ii, X. Li, N. Marquez Peraca, X. Ma, Z. Jin, W. Ren, G. Ma, I. Katayama, J. Takeda, H. Nojiri, D. Turchinovich, S. Cao, M. Bamba, and J. Kono, Ultrastrong magnon–magnon coupling dominated by antiresonant interactions, Nat. Commun. **12**, 3115 (2021).

[44] W. Li, Y. Dai, L. Ni, B. Zhang, D. Tang, Y. Yang, and Y. Xu, Ultrastrong magnon–magnon coupling and chirality switching in antiferromagnet $CrPS_4$, Adv. Funct. Mater. **33**, 2303781 (2023).

[45] A. Sud, K. Yamamoto, K. Z. Suzuki, S. Mizukami, and H. Kurebayashi, Magnon-magnon coupling in synthetic ferrimagnets, Phys. Rev. B **108**, 104407 (2023).

[46] H. Huebl, C. W. Zollitsch, J. Lotze, F. Hocke, M. Greifenstein, A. Marx, R. Gross, and S. T. B. Goennenwein, High cooperativity in coupled microwave resonator ferrimagnetic insulator hybrids, Phys. Rev. Lett. **111**, 127003 (2013).

[47] Y. Tabuchi, S. Ishino, T. Ishikawa, R. Yamazaki, K. Usami, and Y. Nakamura, Hybridizing ferromagnetic magnons and microwave photons in the quantum limit, Phys. Rev. Lett. **113**, 083603 (2014).

[48] X. Zhang, C.-L. Zou, L. Jiang, and H. X. Tang, Strongly coupled magnons and cavity microwave photons, Phys. Rev. Lett. **113**, 156401 (2014).

[49] D. Lachance-Quirion, Y. Tabuchi, A. Gloppe, K. Usami, and Y. Nakamura, Hybrid quantum systems based on magnonics, Appl. Phys. Express **12**, 070101 (2019).

[50] D. D. Awschalom, C. R. Du, R. He, F. J. Heremans, A. Hoffmann, J. Hou, H. Kurebayashi, Y. Li, L. Liu, V. Novosad, J. Sklenar, S. E. Sullivan, D. Sun, H. Tang, V. Tyberkevych, C. Trevillian, A. W. Tsen, L. R. Weiss, W. Zhang, X. Zhang, L. Zhao, and C. W. Zollitsch, Quantum engineering with hybrid magnonic systems and materials, IEEE Trans. Quantum Eng. **2**, 1 (2021).

[51] P. Forn-Díaz, L. Lamata, E. Rico, J. Kono, and E. Solano, Ultrastrong coupling regimes of light-matter interaction, Rev. Mod. Phys. **91**, 025005 (2019).

[52] A. Frisk Kockum, A. Miranowicz, S. De Liberato, S. Savasta, and F. Nori, Ultrastrong coupling between light and matter, Nat. Rev. Phys. **1**, 19 (2019).

[53] A. H. Comstock, C.-T. Chou, Z. Wang, T. Wang, R. Song, J. Sklenar, A. Amassian, W. Zhang, H. Lu, L. Liu, M. C. Beard, and D. Sun, Hybrid magnonics in hybrid perovskite antiferromagnets, Nat. Commun. **14**, 1834 (2023).

[54] See Supplemental Material at http://link.aps.org/supplemental/10.1103/PhysRevB.109.054416 for more details of the formulas and the coupling properties.

[55] C. Ciuti, G. Bastard, and I. Carusotto, Quantum vacuum properties of the intersubband cavity polariton field, Phys. Rev. B **72**, 115303 (2005).

[56] T. Niemczyk, F. Deppe, H. Huebl, E. P. Menzel, F. Hocke, M. J. Schwarz, J. J. Garcia-Ripoll, D. Zueco, T. Hümmer, E. Solano, A. Marx, and R. Gross, Circuit quantum electrodynamics in the ultrastrong-coupling regime, Nat. Phys. **6**, 772 (2010).

[57] Y. Todorov, A. M. Andrews, R. Colombelli, S. De Liberato, C. Ciuti, P. Klang, G. Strasser, and C. Sirtori, Ultrastrong light-matter coupling regime with polariton dots, Phys. Rev. Lett. **105**, 196402 (2010).

[58] A. Baker, M. Beg, G. Ashton, M. Albert, D. Chernyshenko, W. Wang, S. Zhang, M.-A. Bisotti, M. Franchin, C. L. Hu, R. Stamps, T. Hesjedal, and H. Fangohr, Proposal of a micromagnetic standard problem for ferromagnetic resonance simulations, J. Magn. Magn. Mater. **421**, 428 (2017).

[59] G. H. O. Daalderop, P. J. Kelly, and F. J. A. den Broeder, Prediction and confirmation of perpendicular magnetic anisotropy in Co/Ni multilayers, Phys. Rev. Lett. **68**, 682 (1992).

[60] S. Mizukami, X. M. Zhang, T. Kubota, H. Naganuma, M. Oogane, Y. Ando, and T. Miyazaki, Gilbert damping in Ni/Co multilayer films exhibiting large perpendicular anisotropy, Appl. Phys. Express **4**, 013005 (2011).

[61] L. You, R. C. Sousa, S. Bandiera, B. Rodmacq, and B. Dieny, Co/Ni multilayers with perpendicular anisotropy for spintronic device applications, Appl. Phys. Lett. **100**, 172411 (2012).

[62] H. Ohno, D. Chiba, F. Matsukura, T. Omiya, E. Abe, T. Dietl, Y. Ohno, and K. Ohtani, Electric-field control of ferromagnetism, Nature (London) **408**, 944 (2000).

[63] T. Maruyama, Y. Shiota, T. Nozaki, K. Ohta, N. Toda, M. Mizuguchi, A. A. Tulapurkar, T. Shinjo, M. Shiraishi, S. Mizukami, Y. Ando, and Y. Suzuki, Large voltage-induced magnetic anisotropy change in a few atomic layers of iron, Nat. Nanotechnol. **4**, 158 (2009).

[64] J.-G. Choi, J. Park, M.-G. Kang, D. Kim, J.-S. Rieh, K.-J. Lee, K.-J. Kim, and B.-G. Park, Voltage-driven gigahertz frequency tuning of spin Hall nano-oscillators, Nat. Commun. **13**, 3783 (2022).